The role of diffuse electron precipitation in the formation of subauroral polarization streams

Dong Lin[1], Kareem Sorathia[2], Wenbin Wang[1], Viacheslav Merkin[2], Shanshan Bao[3], Kevin Pham[1], Frank Toffoletto[3], Xueling Shi[4,1], Adam Michael[2], John Lyon[5], Jeffrey Garretson[2], and Brian Anderson[2]

[1]High Altitude Observatory, National Center for Atmospheric Research, Boulder CO
[2]Applied Physics Laboratory, Johns Hopkins University, Laurel MD
[3]Department of Physics and Astronomy, Rice University, Houston TX
[4]Bradley Department of Electrical and Computer Engineering, Virginia Tech, Blacksburg VA
[5]Department of Physics and Astronomy, Dartmouth College, Hanover NH

Key Points:

- Physics-based diffuse electron precipitation is implemented in a fully coupled magnetosphere-ionosphere-thermosphere model.
- Diffuse electron precipitation plays a key role in determining the location and structure of subauroral polarization streams.
- Subauroral polarization streams form between the inner edges of the proton ring current and electron plasmasheet.

Corresponding author: Dong Lin, ldong@ucar.edu

Abstract

The role of diffuse electron precipitation in forming subauroral polarization streams (SAPS) is investigated with the Multiscale Atmosphere-Geospace Environment (MAGE) model. Diffuse precipitation is derived from the distribution of drifting electrons calculated in MAGE. SAPS manifest themselves as a separate mesoscale flow channel in the duskside ionosphere when diffuse precipitation is implemented in MAGE, whereas it merges with the primary auroral convection when diffuse precipitation is turned off. SAPS overlap with the downward Region-2 field-aligned currents equatorward of diffuse precipitation, where poleward electric fields closing the Pedersen currents are strong due to a low conductance in the subauroral ionosphere. The Region-2 field-aligned currents extend to lower latitudes than diffuse precipitation because the ring current protons penetrate closer to the Earth than the electrons do. This study demonstrates the critical role of diffuse electron precipitation in determining SAPS location and structure.

Plain Language Summary

[Subauroral polarization streams (SAPS) are a mesoscale (∼100-500 km) plasma flow channel frequently observed in the duskside subauroral ionosphere. This study investigates how diffuse electron precipitation affects the location and structure of SAPS, enabled by the newly developed model capability to directly simulate diffuse precipitation using particle drift physics in a state-of-the-art geospace model called MAGE. Numerical experiments show that SAPS are a separate flow channel when diffuse precipitation is included in the simulation, but they merge with the primary auroral convection when diffuse precipitation is off. SAPS are produced in the gap between the low latitude boundaries of electron aurora and downward field-aligned current (FAC) on the duskside, where the ionospheric conductance is low due to lack of ionization while substantial downward region-2 FAC requires closure. Strong poleward electric fields are generated to drive the enhanced westward ion drifts of SAPS. Tracing back to the magnetosphere, the gap between inner boundaries is formed because the ring current protons, whose distribution primarily determines the downward FAC, penetrate deeper than the electrons, the source population of diffuse precipitation. This study demonstrates the importance of including diffuse precipitation in coupled geospace models to understand the dynamics of mesoscale SAPS structures.]

1 Introduction

Auroral precipitation plays a significant role in the magnetosphere-ionosphere-thermosphere (MIT) coupling by enhancing ionospheric ionization and conductivity at high latitudes (e.g., Hardy et al., 1987). Since MIT electrodynamic coupling depends strongly on the ionospheric conductance (e.g., Hill et al., 1976; Southwood & Wolf, 1978; Foster et al., 1986; Merkin et al., 2003, 2005; Jensen et al., 2017), auroral precipitation affects global ionospheric plasma convection. Among the various types of auroral precipitation that have been identified from satellite measurements, diffuse electron precipitation is the most commonly detected and makes the largest contribution to the total precipitation budget (Newell et al., 2009). The statistical study of Newell et al. (2009) showed that diffuse precipitation contributes up to $\sim 60\%$ of the total precipitation energy flux under both weak and strong solar wind driving conditions. The empirical orthogonal function analysis of McGranaghan et al. (2015) revealed that diffuse precipitation is responsible for the mean pattern and principle variability of ionospheric conductance. Therefore, the distribution of diffuse precipitation is expected to have important impacts on the ionospheric convection and MI coupling processes.

The subauroral polarization streams (SAPS) are mesoscale (∼100 to 500 km at ionospheric altitudes) structures that are frequently observed in the duskside ionosphere. SAPS manifest themselves as a latitudinally narrow, high-speed, westward plasma flow chan-

nel (∼1-5 degrees) equatorward of the low latitude electron auroral boundary (e.g., Foster & Vo, 2002). Previous studies have shown that SAPS represent sophisticated MIT coupling processes that require synergistic investigations of the interactions between solar wind, outer and inner magnetosphere, and ionosphere-thermosphere (e.g., Ebihara et al., 2009; Wang et al., 2012; Califf et al., 2016; Kunduri et al., 2017; He et al., 2017; Yuan et al., 2017; Huang, 2020). Coupled geospace models provide a more comprehensive and self-consistent view of SAPS in the context of MIT coupling (e.g., Yu et al., 2015; Raeder et al., 2016; Lin et al., 2019) compared to empirical or prescribed specification of SAPS in standalone magnetospheric and ionospheric models (e.g., Zheng et al., 2008; Wang et al., 2012; Guo et al., 2018; Ferdousi et al., 2019). Although existing coupled geospace models provide overall reasonable representations of the global ionospheric convection pattern, it is still challenging for them to fully reproduce the physics of SAPS, particularly at mesoscales. For example, Lin et al. (2019) used a coupled MIT model to simulate SAPS during the 17 March 2013 geomagnetic storm. The SAPS channel was not discernible from the auroral convection compared with Defense Meteorology Satellite Program (DMSP) measurements, which was attributed to the lack of a faithful representation of the diffuse aurora.

Diffuse electron precipitation is determined by the plasmasheet distribution of electrons that are deposited into the ionosphere-thermosphere (Ni et al., 2016). Global magnetohydrodynamic (MHD) models of the magnetosphere traditionally implement auroral precipitation via empirical parameterization of MHD variables of plasma density, temperature, and field-aligned current (FAC) (e.g., Fedder et al., 1995; Raeder et al., 2001). However, diffuse precipitation obtained from an MHD parameterization intrinsically lacks some key features of the source electron population that are caused by their energy-dependent drifts, not included in MHD models, e.g., dawn-dusk asymmetry. In order to obtain a diffuse precipitation distribution consistent with the statistics of Newell et al. (2009), Zhang et al. (2015) introduced an empirical diffuse precipitation mask in a global MHD magnetospheric model to represent the eastward drift of electrons, which lacked self-consistency and dynamic variability. Ring current models have been recently used to derive diffuse electron precipitation based on kinetic physics (e.g. Fok et al., 2014; Chen et al., 2015; Yu et al., 2016). For example, Yu et al. (2016) calculated the pitch angle diffusion coefficients associated with whistler mode chorus and hiss waves, which resulted in diffuse electron precipitation in better agreement with satellite measurements than MHD-based results.

This study focuses on the influence of diffuse electron precipitation on MIT coupling with a particular emphasis on mesoscale SAPS structure. In order to systematically understand its role, diffuse precipitation is implemented in a fully coupled geospace model by making use of electron distribution determined by tracking their energy-dependent drifts. In the newly developed Multiscale Atmosphere-Geospace Environment (MAGE) model, diffuse electron precipitation is derived from the electron distribution in a ring current model, which solves for the bounce-averaged drifts of particles. The diffuse precipitation together with MHD-based mono-energetic electron precipitation are input to a general circulation ionosphere-thermosphere (IT) model to characterize the IT response and feedback. SAPS in the 17 March 2013 geomagnetic storm event are revisited with the MAGE model. The drift physics-informed precipitation and the fully coupled geospace model of MAGE, as will be elaborated in this paper, represent an important advance in characterizing auroral precipitation in geospace models and show significant improvements in resolving SAPS at mesoscales. Using the fully coupled first-principles MAGE model, we illustrate the formation of SAPS as a manifestation of the collective dynamic behavior of the coupled MIT system.

Figure 1. (a) Diagram of the MAGE model. (b-f) Solar wind/IMF and SYMH index for 17 March 2013 from CDAWeb OMNI data product.

2 Model Description

MAGE is a coupled model for simulating the geospace system, developed at the NASA DRIVE Science Center for Geospace Storms. This study is based on the current iteration of the MAGE model, whose diagram is illustrated in Figure 1a. MAGE consists of the Grid Agnostic MHD with Extended Research Applications (GAMERA) global MHD model of the magnetosphere (Zhang et al., 2019a; Sorathia et al., 2020), the Rice Convection Model (RCM) model of the ring current (Toffoletto et al., 2003), Thermosphere-Ionosphere Electrodynamics General Circulation Model (TIEGCM) of the upper atmosphere (Richmond et al., 1992), and RE-developed Magnetosphere-Ionosphere Coupler/Solver (REMIX) (Merkin & Lyon, 2010). GAMERA carries on the legacy of its predecessor, the Lyon-Fedder-Mobbary (LFM) model (Lyon et al., 2004) as described by (Sorathia et al., 2020). The coupling between the different MAGE components is conceptually similar to the previous coupled geospace model developed by the same group (e.g., Lin et

al., 2019), but the software implementation is entirely new and will be described in more detail elsewhere.

MAGE implements an electron precipitation model that takes into account the distinct physical driving mechanisms for the diffuse and mono-energetic electron precipitation. As illustrated in Figure 1a, mono-energetic electron precipitation is derived from MHD density, temperature, and FAC on the inner boundary of GAMERA (at two Earth radii) based on the formulation of Zhang et al. (2015). Only the precipitation that undergoes field-aligned electrostatic potential drop is adopted as the mono-energetic electron precipitation in MAGE. Precipitation anywhere else is treated as diffuse electron precipitation and uses the results derived from RCM, which solves bounce-averaged drift motion of ring current electrons and ions. The diffuse precipitation is calculated by integrating the electron distribution function in RCM and assuming that the precipitation loss rate is one third of that derived from strong pitch angle scattering (Wolf, 1983; Schumaker et al., 1989; Bao, 2019). These two types of precipitating electrons (mono-energetic and diffuse) are combined in REMIX and passed to TIEGCM to calculate ionospheric ionization rate and electron density, the magnitude and distribution of ionospheric conductivity, and height-integrated conductance. RCM has also been improved in MAGE to include a zero-energy channel to model the cold plasmaspheric mass. The dynamic plasmasphere is initialized with the Gallagher empirical model (Gallagher et al., 1988) and then evolved self-consistently using the electrostatic potential from REMIX with added corotation. This improvement to RCM will be described in detail elsewhere.

In this study, GAMERA uses $96 \times 96 \times 128$ grid cells in the radial, meridional, and azimuthal directions, respectively, where the spherical symmetry axis of the grid is pointing from Earth to Sun. RCM uses $200 \times 100 \times 90$ grid cells in the latitudinal, longitudinal (in Solar Magnetic, SM, coordinates), and energy dimensions, respectively. In the energy dimension, 27 energy channels are for electrons, 62 energy channels for protons, and 1 zero-energy channel for the cold plasmasphere. REMIX grid uses 45×360 grid cells in the latitudinal and longitudinal directions (in SM), respectively. Its resolution is 1° in both dimensions and the low latitude boundary is at 45° magnetic latitude (MLAT). TIEGCM uses $288 \times 144 \times 57$ cells in longitudinal, latitudinal, and altitudinal directions (in geographic coordinate system), respectively. It has a uniform horizontal resolution of 1.25° and a vertical pressure grid of 0.25 scale height. GAMERA and TIEGCM both adopt a ring-average technique to treat the spherical axis of their respective grids (Zhang et al., 2019b; Dang et al., 2020). GAMERA and RCM exchange information every 15 s, GAMERA and REMIX every 5 s, and REMIX and TIEGCM every 5 s.

3 Data-Model Comparison

MAGE is used to simulate the well-known St. Patrick's Day geomagnetic storm on 17 March 2013. The solar wind and IMF conditions to drive the simulation are shown in Figure 1b-1e, which are obtained from the CDAWeb OMNI data product with 1 minute resolution. OMNI data gaps are filled with linear interpolation. The geomagnetic storm was triggered by a coronal mass ejection (CME) which arrived at Earth at 05:55 UT. The solar wind density increased to 10 cm^{-3} and solar wind V_X to 700 km/s across the CME shock. During the storm the IMF B_Z component was mostly southward with occasional northward turnings, the strongest B_Z was nearly -20 nT. The SYMH index dropped to below -100 nT in the main phase.

SAPS structures are analyzed by comparing the simulation results with observational data. Figure 2 shows DMSP F18 measurements during three duskside auroral crossings in black curves. MAGE simulation results are sampled along the F18 trajectory and shown in red curves. From top to bottom the rows show the integrated electron precipitation energy flux (EnFlux), horizontal ion drifts along the cross track direction of DMSP

F18 (V_{HD}), FAC density (positive downward), and Pedersen conductance (Σ_P). DMSP EnFlux and V_{HD} are smoothed with a 15 s moving mean of the original 1 s resolution data. The DMSP FACs are smoothed with a 60 s moving mean of the 1 s resolution results provided by Xiong et al. (2020). MAGE results are output by REMIX every 15 s.

The electron auroral equatorward boundary is defined where EnFlux drops to 10% of the peak value in each crossing. For example, during the crossing between 08:28 and 08:38 UT (Figure 2a) MAGE simulated electron auroral equatorward boundary was at $\sim 62°$ MLAT, as indicated by the vertical blue dashed line in the first column. To the left of the blue line is the subauroral region shaded in magenta. The DMSP-measured electron auroral equatorward boundary was located at $\sim 65°$ MLAT by referring to the black curve in Figure 2a. Figure 2b compares the simulated and measured V_{HD} during the 08:28-08:38 UT auroral crossing. The subauroral flow channel occurs below 62° MLAT in the MAGE results (note the secondary bump in the red trace), which is identified as SAPS. DMSP measured V_{HD} also shows a SAPS channel below $\sim 63°$ MLAT. During this auroral crossing, downward FACs are seen between $\sim 55°$ and $63-64°$ MLAT (Figure 2c). Here downward FACs are defined as positive in both hemispheres, shaded in green. Note DMSP measured FACs almost overlap with the MAGE FACs. The magenta and green shaded regions in Figure 2b reveal that the SAPS channel is mostly sandwiched by the equatorward boundaries of electron aurora and downward FAC. Figure 2d shows the MAGE simulated Σ_P which drops dramatically equatorward of the electron precipitation boundary.

The right two columns of Figure 2 show MAGE-DMSP comparison in the same format for two other auroral crossings in the duskside southern hemisphere during 11:18-11:28 UT and 13:00-13:10 UT, respectively. The simulated SAPS locations are very close to those from DMSP measurements. Although the peak magnitudes are sometimes different by a few hundred m/s, the MAGE-simulated latitudinal structures of ion drifts in these three examples are similar to those in the DMSP data and reveal the SAPS channel unambiguously. A comparison of FAC with Active Magnetosphere and Planetary Electrodynamics Response Experiment (AMPERE) measurements also validates the spatial distribution of large-scale FAC from the simulation results, which are shown in the Supporting Information (Figure S1).

The sampled EnFlux from MAGE is mostly diffuse precipitation during the crossing between 08:28 UT and 08:38 UT although DMSP energy spectrum shows mono-energetic precipitation features for that single peak collocated with upward FAC. Two EnFlux peaks were detected by DSMP and simulated by MAGE during the crossing between 11:18 UT and 11:28 UT. The equatorward one is diffuse precipitation and the poleward one was mono-energetic precipitation. During the auroral crossing from 13:00 UT to 13:10 UT DMSP F18 detected three EnFlux peaks, the most equatorward one was diffuse precipitation while the poleward two were mono-energetic precipitation associated with upward FAC structures. Additional comparison of EnFlux and V_{HD} between MAGE simulations and multiple DMSP satellite measurements is provided in the Supporting Information (Movie S1).

In order to better understand the role of diffuse precipitation in generating and shaping SAPS, a controlled experiment was conducted by turning off diffuse precipitation in the MAGE model and compared with the baseline run including diffuse precipitation shown in Figure 2. Figure 3 shows the simulation results at 11:10 UT from the baseline run in the top row and from the run with diffuse precipitation off in the bottom row. The first three columns from left to right show EnFlux, FAC, and westward ion drifts (WID) in the northern hemisphere ionosphere output by REMIX, respectively. The magenta curves show EnFlux contour level of 1.0 mW/m^2 and are used to indicate the auroral boundaries. The green curves show FAC contour level of 0.2 μA/m^2 and indicate the downward FAC boundaries. The two boundaries are over-plotted on top of WID in Figures 3c and 3g.

Figures 3d and 3h show the latitudinal distributions of EnFlux, FAC, and WID with magenta, green, and blue curves, respectively, which are sampled across MLAT at 20 hours magnetic local time (MLT). Figure 3d shows a mono-energetic electron precipitation peak at around 70° MLAT and a diffuse precipitation peak at around 62° MLAT in the baseline run. Diffuse precipitation is located in the high latitude part of the downward Region 2 (R2) FAC. A SAPS channel is clearly visible between $\sim$ 53° and 58° MLAT with a peak velocity of $\sim$ 1.3 km/s at $\sim$ 56° MLAT. This SAPS channel is equatorward of the diffuse precipitation and in the downward R2 FAC region. In the run with diffuse precipitation turned off (Figure 3h), there is only one auroral band consisting of mono-energetic electron precipitation and collocated with the upward (negative) FAC. The subauroral convection is nearly 20° broad latitudinally from $\sim$ 53° to $\sim$ 73° MLAT.

The two-dimensional distributions of ionospheric convection and their relative locations to EnFlux and FAC in these two model runs are illustrated in Figure 3a-3c, 3e-3g. Figure 3a shows that in the baseline run, the electron auroral equatorward boundary is located at around 64° MLAT from 16 to 19 MLT and at around 60° MLAT from 19 MLT through the dawnside to 12 MLT. With diffuse precipitation off, the electron auroral equatorward boundary is at around 70° MLAT, above which mono-energetic electron precipitation is concentrated in the duskside upward Region 1 (R1) FAC (Figure 3e). It is the diffuse precipitation that moves the electron auroral equatorward boundary to a lower latitude in the MLT sector from post-dusk to dawn. Figure 3c shows SAPS as a separate enhanced westward flow channel inside the R2 FAC in the dusk sector. In the run with diffuse precipitation off, however, the auroral equatorward boundary is at a much higher latitude and subauroral plasma convection spans more than 10° in latitude and exhibits no mesoscale SAPS structure evident in Figure 3g.

SAPS are generated in the subauroral region as a result of current closure. Equatorward of the auroral precipitation, the ionospheric conductance drops dramatically due to lack of precipitating particles to ionize the neutral atmosphere, especially after sunset when solar radiation vanishes. Such latitudinal variations of Σ_P are verified in the MAGE simulation and shown in Figures 2d, 2h, and 2l. However, since the equatorward boundary of downward FAC is at a lower latitude than the electron precipitation low latitude boundary, there are still substantial R2 FACs that need to be closed in the gap between the two low latitude boundaries (Figure 3c). Due to Ohm's law, the relatively low conductance between the two boundaries results in an enhanced poleward electric field to drive the Pedersen currents to flow poleward. That strong electric field then produces enhanced westward ion drifts (SAPS) in the subauroral region.

The gap between the equatorward boundaries of FAC and EnFlux can be traced back to the magnetosphere. Figure 4 illustrates the SAPS driving mechanism from the perspective of the coupled magnetosphere-ionosphere. The ionospheric zonal ion drifts are shown on the white hemisphere with a red-blue colormap, where red indicates westward drifts. The inset presents an amplified view of the SAPS channel in the dusk sector, which is sandwiched by the low latitude boundaries of electron precipitation (magenta) and downward FAC (green). The boundaries are mapped along the geomagnetic field lines to the magnetospheric equatorial plane, where the plasma density is represented with a purple-yellow colormap. The semi-transparent surfaces show the near-equatorial part of the geomagnetic field lines connecting the EnFlux/FAC boundaries in the magnetosphere and ionosphere. The gap between the ionospheric low latitude boundaries of EnFlux and downward FAC is projected to the region between their inner boundaries in the equatorial plane, as pointed out by the blue arrows. In the magnetospheric plasmasheet, downward FAC is primarily determined by the ion pressure distribution while the electron precipitation is uniquely populated by the electron distribution. Since plasmasheet ions typically penetrate deeper than the electrons, the inner edge of the ion distribution is more inward than the electrons (e.g. Califf et al., 2016). The downward FAC

inner boundary is therefore more inward than that of the electron precipitation, which forms the gap region where SAPS are generated.

4 Conclusion and Discussion

In this study we explored the role of diffuse electron precipitation in the formation of SAPS using the state-of-the-art coupled geospace model, MAGE. Diffuse precipitation is derived from the electron distribution solved for by the RCM component of MAGE. The diffuse precipitation, informed by the ring current model including energy-dependent drifts, is an important advance in characterizing the major component of auroral precipitation in geospace models compared to the traditional approach of MHD-based parameterizations. The particle distribution-based diffuse precipitation and MHD-based mono-energetic electron precipitation are combined as inputs for an ionosphere-thermosphere model to calculate ionospheric conductance, which is done here for the first time in a fully coupled geospace model. MAGE simulation results of the 17 March 2013 geomagnetic storm captured unambiguous SAPS structures that are in a good agreement with DMSP F18 measurements. Controlled numerical experiments further demonstrate the critical role of diffuse precipitation in the formation of SAPS, i.e. SAPS manifest themselves as a separate subauroral flow channel when diffuse precipitation is included in the simulation whereas they merge with the primary auroral convection when the diffuse precipitation is turned off. The driving mechanism of SAPS is illustrated from the perspective of coupled magnetosphere-ionosphere. Since the ring current protons penetrate deeper than the electrons in the duskside inner magnetosphere, the inner edge of proton ring current is closer to the Earth than the inner edge of the electron plasmasheet. When mapped to the duskside ionosphere, the equatorward boundary of downward FAC is below that of the electron precipitation, leaving R2 FAC requiring closure in the low conductance subauroral region. An enhanced poleward electric field is generated to drive the high speed westward plasma flow of SAPS (Anderson et al., 2001).

This investigation on how the diffuse electron precipitation impacts the formation of SAPS is enabled by the new modeling capabilities developed in MAGE. Diffuse precipitation is directly derived from the electron distribution function in the RCM which tracks the energy-dependent particle drifts. The resultant diffuse precipitation shows a natural dawnward rotation due to the eastward drift of electrons in the inner magnetosphere (Figure 3a), which is intrinsically absent in the MHD description. An even more sophisticated diffuse precipitation has been recently derived from a kinetic ring current model by taking into account wave-particle interactions (Yu et al., 2016). In this paper, we take a further step in improving the physical description of diffuse precipitation in the MIT system by coupling to a physics-based model of the ionosphere-thermosphere, which computes the ionospheric conductivity self-consistently, given the precipitating electron fluxes. This, in turn, enabled a comprehensive investigation of SAPS, which requires all of the ingredients included in our model simultaneously: a ring current model, which correctly tracks the electron and ion drifts and the earthward boundaries of their magnetospheric distributions, in combination with a self-consistent ionosphere-magnetosphere model.

Our results suggest a number of further improvements to the MAGE model. The comparison with DMSP measurements (Figure 2) indicates that the model resolution is still not sufficient to capture the observed variability of the ionospheric precipitation, FACs and convection. While the individual MAGE components have been run at a significantly higher resolution separately (e.g., Sorathia et al., 2020; Dang et al., 2020), such a high-resolution coupled MAGE simulation is currently in development. Furthermore, SAPS are missed toward the dayside in the model when comparing with DMSP F16 and F17, which crossed the duskside auroral oval closer to noon, as shown in the Supporting Information. This can be attributed to the underestimated precipitation in the postnoon sector, implying the uniform electron loss rate in RCM may be oversimplified. Fi-

nally, currently only mono-energetic electron precipitation and diffuse precipitation are implemented in the MAGE precipitation model, which is justified as a first step by their statistically dominant contribution to the total precipitation energy and number flux (Newell et al., 2009). However, other types of precipitation such as ion precipitation can also play a role in the generation of localized structures and dynamics, especially in the subauroral SAPS region (e.g. Yuan et al., 2016). These particle and energy inputs will be included in the future iterations of the MAGE model.

Acknowledgments

Dong Lin is supported by the Advanced Study Program (ASP) Postdoctoral Fellowship of National Center for Atmospheric Research (NCAR). NCAR is sponsored by National Science Foundation (NSF). This work is supported by NASA GCR grant 80NSSC17K0013, LWS grants 80NSSC20K0356 and 80NSSC19K0080, the DRIVE Science Center for Geospace Storms (CGS) under grant 80NSSC20K0601, NASA O2R grant 80NSSC19K0241, and NCAR System for Integrated Modeling of the Atmosphere (SIMA) reinvestment fund. We would like to acknowledge high-performance computing support from Cheyenne (doi:10.5065/D6RX99HX) provided by NCAR's Computational and Information Systems Laboratory. Dong Lin is thankful to Dr. Simon Wing and Dr. Thomas Sotirelis for the discussions on DMSP data, to Dr. Chao Xiong for the DMSP FAC results, and to Dr. Gang Lu for the internal review. The OMNI data are available at https://cdaweb.gsfc.nasa.gov/index.html/. The DMSP SSJ and SSIES data are obtained from https://satdat.ngdc.noaa.gov/dmsp/data/ and FAC data from ftp://magftp.gfz-potsdam.de/DMSP/FAC/. The AMPERE data are obtained from http://ampere.jhuapl.edu/. The simulation data are archived in https://doi.org/10.5065/xaz4-cc27.

References

Anderson, P., Carpenter, D., Tsuruda, K., Mukai, T., & Rich, F. (2001). Multisatellite observations of rapid subauroral ion drifts (SAID). *Journal of Geophysical Research: Space Physics*, *106*(A12), 29585–29599. doi: 10.1029/2001JA000128

Bao, S. (2019). *Large-scale coupled models of the inner magnetosphere* (Doctoral dissertation, Rice University). doi: https://hdl.handle.net/1911/107801

Califf, S., Li, X., Wolf, R., Zhao, H., Jaynes, A., Wilder, F., ... Redmon, R. (2016). Large-amplitude electric fields in the inner magnetosphere: Van Allen Probes observations of subauroral polarization streams. *Journal of Geophysical Research: Space Physics*, *121*(6), 5294–5306. doi: 10.1002/2015JA022252

Chen, M. W., Lemon, C. L., Orlova, K., Shprits, Y., Hecht, J., & Walterscheid, R. (2015). Comparison of simulated and observed trapped and precipitating electron fluxes during a magnetic storm. *Geophysical Research Letters*, *42*(20), 8302–8311. doi: 10.1002/2015GL065737

Dang, T., Zhang, B., Lei, J., Wang, W., Burns, A., Liu, H.-l., ... Sorathia, K. A. (2020). Development of high-resolution thermosphere–ionosphere electrodynamics general circulation model (TIE-GCM) using ring average technique. *Geoscientific Model Development Discussions*, 1–30. doi: 10.5194/gmd-2020-243

Ebihara, Y., Nishitani, N., Kikuchi, T., Ogawa, T., Hosokawa, K., Fok, M.-C., & Thomsen, M. (2009). Dynamical property of storm time subauroral rapid flows as a manifestation of complex structures of the plasma pressure in the inner magnetosphere. *Journal of Geophysical Research: Space Physics*, *114*(A1). doi: 10.1029/2008JA013614

Fedder, J. A., Slinker, S. P., Lyon, J. G., & Elphinstone, R. (1995). Global numerical simulation of the growth phase and the expansion onset for a substorm observed by Viking. *Journal of Geophysical Research: Space Physics*, *100*(A10),

19083–19093. doi: 10.1029/95JA01524

Ferdousi, B., Nishimura, Y., Maruyama, N., & Lyons, L. R. (2019). Subauroral neutral wind driving and its feedback to SAPS during the 17 March 2013 geomagnetic storm. *Journal of Geophysical Research: Space Physics*, *124*(3), 2323–2337. doi: 10.1029/2018JA026193

Fok, M.-C., Buzulukova, N., Chen, S.-H., Glocer, A., Nagai, T., Valek, P., & Perez, J. (2014). The comprehensive inner magnetosphere-ionosphere model. *Journal of Geophysical Research: Space Physics*, *119*(9), 7522–7540. doi: 10.1002/2014JA020239

Foster, J., Holt, J. M., Musgrove, R., & Evans, D. (1986). Ionospheric convection associated with discrete levels of particle precipitation. *Geophysical Research Letters*, *13*(7), 656–659. doi: 10.1029/GL013i007p00656

Foster, J., & Vo, H. (2002). Average characteristics and activity dependence of the subauroral polarization stream. *Journal of Geophysical Research: Space Physics*, *107*(A12), SIA–16. doi: 10.1029/2002JA009409

Gallagher, D., Craven, P., & Comfort, R. (1988). An empirical model of the Earth's plasmasphere. *Advances in space research*, *8*(8), 15–24. doi: 10.1016/0273-1177(88)90258-X

Guo, J.-P., Deng, Y., Zhang, D.-H., Lu, Y., Sheng, C., & Zhang, S.-R. (2018). The effect of subauroral polarization streams on ionosphere and thermosphere during the 2015 St. Patrick's Day storm: Global ionosphere-thermosphere model simulations. *Journal of Geophysical Research: Space Physics*, *123*(3), 2241–2256. doi: 10.1002/2017JA024781

Hardy, D. A., Gussenhoven, M., Raistrick, R., & McNeil, W. (1987). Statistical and functional representations of the pattern of auroral energy flux, number flux, and conductivity. *Journal of Geophysical Research: Space Physics*, *92*(A11), 12275–12294. doi: 10.1029/JA092iA11p12275

He, F., Zhang, X.-X., Wang, W., & Wan, W. (2017). Different evolution patterns of subauroral polarization streams (SAPS) during intense storms and quiet time substorms. *Geophysical Research Letters*, *44*(21). doi: 10.1002/2017GL075449

Hill, T., Dessler, A., & Wolf, R. (1976). Mercury and Mars: The role of ionospheric conductivity in the acceleration of magnetospheric particles. *Geophysical Research Letters*, *3*(8), 429–432. doi: 10.1029/GL003i008p00429

Huang, C.-S. (2020). Westward plasma drifts in the nighttime equatorial ionosphere during severe magnetic storms: A new type of penetration electric fields caused by subauroral polarization stream. *Journal of Geophysical Research: Space Physics*, *125*(10), e2020JA028300. doi: 10.1029/2020JA028300

Jensen, J. B., Raeder, J., Maynard, K., & Cramer, W. D. (2017). Particle precipitation effects on convection and the magnetic reconnection rate in Earth's magnetosphere. *Journal of Geophysical Research: Space Physics*, *122*(11), 11–413. doi: 10.1002/2017JA024030

Kunduri, B., Baker, J., Ruohoniemi, J., Thomas, E., Shepherd, S., & Sterne, K. (2017). Statistical characterization of the large-scale structure of the subauroral polarization stream. *Journal of Geophysical Research: Space Physics*, *122*(6), 6035–6048. doi: 10.1002/2017JA024131

Lin, D., Wang, W., Scales, W. A., Pham, K., Liu, J., Zhang, B., ... Maimaiti, M. (2019). SAPS in the 17 March 2013 storm event: Initial results from the coupled magnetosphere-ionosphere-thermosphere model. *Journal of Geophysical Research: Space Physics*, *124*(7), 6212–6225. doi: 10.1029/2019JA026698

Lyon, J., Fedder, J., & Mobarry, C. (2004). The Lyon–Fedder–Mobarry (LFM) global MHD magnetospheric simulation code. *Journal of Atmospheric and Solar-Terrestrial Physics*, *66*(15-16), 1333–1350. doi: 10.1016/j.jastp.2004.03.020

McGranaghan, R., Knipp, D. J., Matsuo, T., Godinez, H., Redmon, R. J., Solomon,

S. C., & Morley, S. K. (2015). Modes of high-latitude auroral conductance variability derived from DMSP energetic electron precipitation observations: Empirical orthogonal function analysis. *Journal of Geophysical Research: Space Physics*, *120*(12), 11–013. doi: 10.1002/2015JA021828

Merkin, V., & Lyon, J. (2010). Effects of the low-latitude ionospheric boundary condition on the global magnetosphere. *Journal of Geophysical Research: Space Physics*, *115*(A10). doi: 10.1029/2010JA015461

Merkin, V., Papadopoulos, K., Milikh, G., Sharma, A., Shao, X., Lyon, J., & Goodrich, C. (2003). Effects of the solar wind electric field and ionospheric conductance on the cross polar cap potential: Results of global MHD modeling. *Geophysical Research Letters*, *30*(23). doi: 10.1029/2003GL017903

Merkin, V., Sharma, A., Papadopoulos, K., Milikh, G., Lyon, J., & Goodrich, C. (2005). Global MHD simulations of the strongly driven magnetosphere: Modeling of the transpolar potential saturation. *Journal of Geophysical Research: Space Physics*, *110*(A9). doi: 10.1029/2004JA010993

Newell, P., Sotirelis, T., & Wing, S. (2009). Diffuse, monoenergetic, and broadband aurora: The global precipitation budget. *Journal of Geophysical Research: Space Physics*, *114*(A9). doi: 10.1029/2009JA014326

Ni, B., Thorne, R. M., Zhang, X., Bortnik, J., Pu, Z., Xie, L., ... others (2016). Origins of the Earths diffuse auroral precipitation. *Space Science Reviews*, *200*(1-4), 205–259. doi: 10.1007/s11214-016-0234-7

Raeder, J., Cramer, W. D., Jensen, J., Fuller-Rowell, T., Maruyama, N., Toffoletto, F., & Vo, H. (2016). Sub-auroral polarization streams: A complex interaction between the magnetosphere, ionosphere, and thermosphere. In *Journal of physics: Conference series* (Vol. 767, p. 012021). doi: 10.1088/1742-6596/767/1/012021

Raeder, J., McPherron, R., Frank, L., Kokubun, S., Lu, G., Mukai, T., ... Slavin, J. (2001). Global simulation of the Geospace Environment Modeling substorm challenge event. *Journal of Geophysical Research: Space Physics*, *106*(A1), 381–395. doi: 10.1029/2000JA000605

Richmond, A., Ridley, E., & Roble, R. (1992). A thermosphere/ionosphere general circulation model with coupled electrodynamics. *Geophysical Research Letters*, *19*(6), 601–604. doi: 10.1029/92GL00401

Schumaker, T. L., Gussenhoven, M. S., Hardy, D. A., & Carovillano, R. L. (1989). The relationship between diffuse auroral and plasma sheet electron distributions near local midnight. *Journal of Geophysical Research: Space Physics*, *94*(A8), 10061–10078. doi: 10.1029/JA094iA08p10061

Sorathia, K., Merkin, V., Panov, E., Zhang, B., Lyon, J., Garretson, J., ... Wiltberger, M. (2020). Ballooning-interchange instability in the near-Earth plasma sheet and auroral beads: Global magnetospheric modeling at the limit of the MHD approximation. *Geophysical research letters*, *47*(14), e2020GL088227. doi: 10.1029/2020GL088227

Southwood, D., & Wolf, R. (1978). An assessment of the role of precipitation in magnetospheric convection. *Journal of Geophysical Research: Space Physics*, *83*(A11), 5227–5232. doi: 10.1029/JA083iA11p05227

Toffoletto, F., Sazykin, S., Spiro, R., & Wolf, R. (2003). Inner magnetospheric modeling with the Rice Convection Model. *Space Science Reviews*, *107*(1-2), 175–196. doi: 10.1023/A:1025532008047

Wang, W., Talaat, E. R., Burns, A. G., Emery, B., Hsieh, S.-y., Lei, J., & Xu, J. (2012). Thermosphere and ionosphere response to subauroral polarization streams (SAPS): Model simulations. *Journal of Geophysical Research: Space Physics*, *117*(A7). doi: 10.1029/2012JA017656

Wolf, R. (1983). The quasi-static (slow-flow) region of the magnetosphere. In *Solar-terrestrial physics* (pp. 303–368). Springer. doi: 10.1007/978-94-009-7194-3_14

Xiong, C., Stolle, C., Alken, P., & Rauberg, J. (2020). Relationship between

large-scale ionospheric field-aligned currents and electron/ion precipitations: DMSP observations. *Earth, Planets and Space*, *72*(1), 1–22. doi: 10.1186/s40623-020-01286-z

Yu, Y., Jordanova, V., Zou, S., Heelis, R., Ruohoniemi, M., & Wygant, J. (2015). Modeling subauroral polarization streams during the 17 March 2013 storm. *Journal of Geophysical Research: Space Physics*, *120*(3), 1738–1750. doi: 10.1002/2014JA020371

Yu, Y., Jordanova, V. K., Ridley, A. J., Albert, J. M., Horne, R. B., & Jeffery, C. A. (2016). A new ionospheric electron precipitation module coupled with RAM-SCB within the geospace general circulation model. *Journal of Geophysical Research: Space Physics*, *121*(9), 8554–8575. doi: 10.1002/2016JA022585

Yuan, Z., Qiao, Z., Li, H., Huang, S., Wang, D., Yu, X., & Yu, T. (2017). Subauroral polarization stream on the outer boundary of the ring current during an energetic ion injection event. *Journal of Geophysical Research: Space Physics*, *122*(4), 4837–4845. doi: 10.1002/2016JA023570

Yuan, Z., Xiong, Y., Qiao, Z., Li, H., Huang, S., Wang, D., ... Wang, J. (2016). A subauroral polarization stream driven by field-aligned currents associated with precipitating energetic ions caused by EMIC waves: A case study. *Journal of Geophysical Research: Space Physics*, *121*(2), 1696–1705. doi: 10.1002/2015JA021804

Zhang, B., Lotko, W., Brambles, O., Wiltberger, M., & Lyon, J. (2015). Electron precipitation models in global magnetosphere simulations. *Journal of Geophysical Research: Space Physics*, *120*(2), 1035–1056. doi: 10.1002/2014JA020615

Zhang, B., Sorathia, K. A., Lyon, J. G., Merkin, V. G., Garretson, J. S., & Wiltberger, M. (2019a). Gamera: A three-dimensional finite-volume MHD solver for non-orthogonal curvilinear geometries. *The Astrophysical Journal Supplement Series*, *244*(1), 20. doi: 10.3847/1538-4365/ab3a4c

Zhang, B., Sorathia, K. A., Lyon, J. G., Merkin, V. G., & Wiltberger, M. (2019b). Conservative averaging-reconstruction techniques (Ring Average) for 3-D finite-volume MHD solvers with axis singularity. *Journal of Computational Physics*, *376*, 276–294. doi: 10.1016/j.jcp.2018.08.020

Zheng, Y., Brandt, P. C., Lui, A. T., & Fok, M.-C. (2008). On ionospheric trough conductance and subauroral polarization streams: Simulation results. *Journal of Geophysical Research: Space Physics*, *113*(A4). doi: 10.1029/2007JA012532

Figure 2. Comparison of DMSP F18 measurements (black) and MAGE simulation results (red) during three duskside auroral crossings. From top to bottom are integrated electron precipitation energy flux (EnFlux), cross track ion drift velocity (V_{HD}), FAC density, and Pedersen conductance (Σ_P). The blue vertical dashed lines indicate the equatorward auroral boundaries in MAGE results, defined as where EnFlux is 0.1 of the peak value in the aurora. The subauroral regions are shaded in magenta. Downward FAC (positive) regions are shaded in green.

Figure 3. Comparison between with (top row) and without (bottom row) diffuse precipitation in MAGE simulations of SAPS. The left three columns are EnFlux, FAC density, and westward ion drifts (WID) in the northern hemisphere ionosphere from REMIX outputs. The magenta curves are EnFlux contour level of 1.0 mW/m^2. The green curves are FAC contour level of 0.2 μA/m^2. WID has the corotation velocity added. The fourth column shows the latitudinal distributions of EnFlux (magenta), FAC (green), and WID (blue) sampled at 20 hours MLT.

Figure 4. SAPS viewed from the ionosphere and magnetosphere. The white hemisphere near the axis origin on top of the orange square represents the northern hemisphere ionosphere. The red-blue colors represent westward and eastward ion drifts, respectively. The high latitude part of the hemisphere is amplified in the inset plot for better visibility. The low latitude one of the two red belts represents SAPS. The purple-yellow colors represent the plasma density distribution in the magnetospheric equatorial plane. The magenta and green curves represent the electron precipitation boundary and duskside downward FAC boundary, respectively. The boundaries in the ionosphere and magnetosphere are connected by geomagnetic field lines, which are partly visualized with the semi-transparent surfaces.

Figure 1.

(a)

MAGE

Multiscale Atmosphere-Geospace Environment

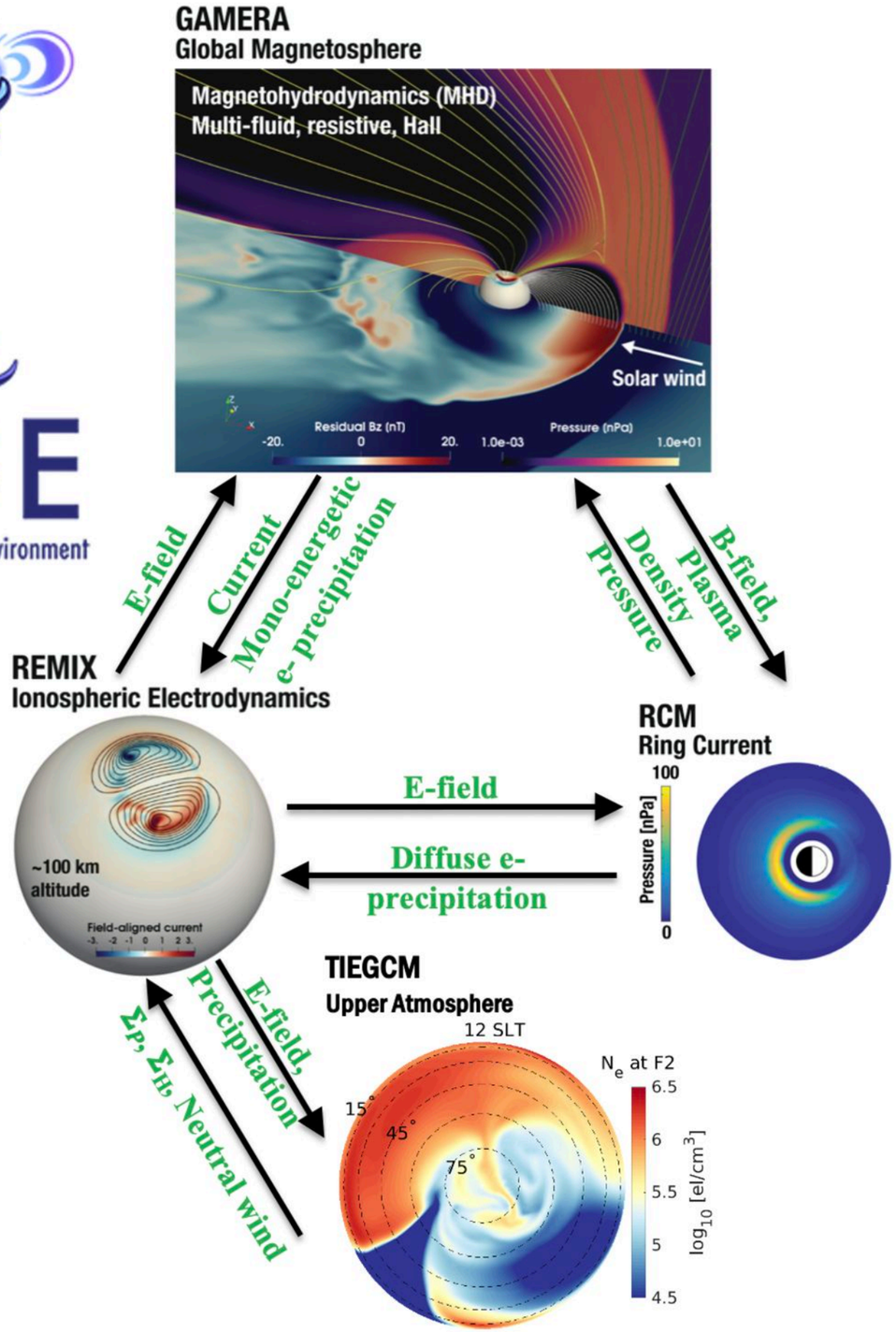

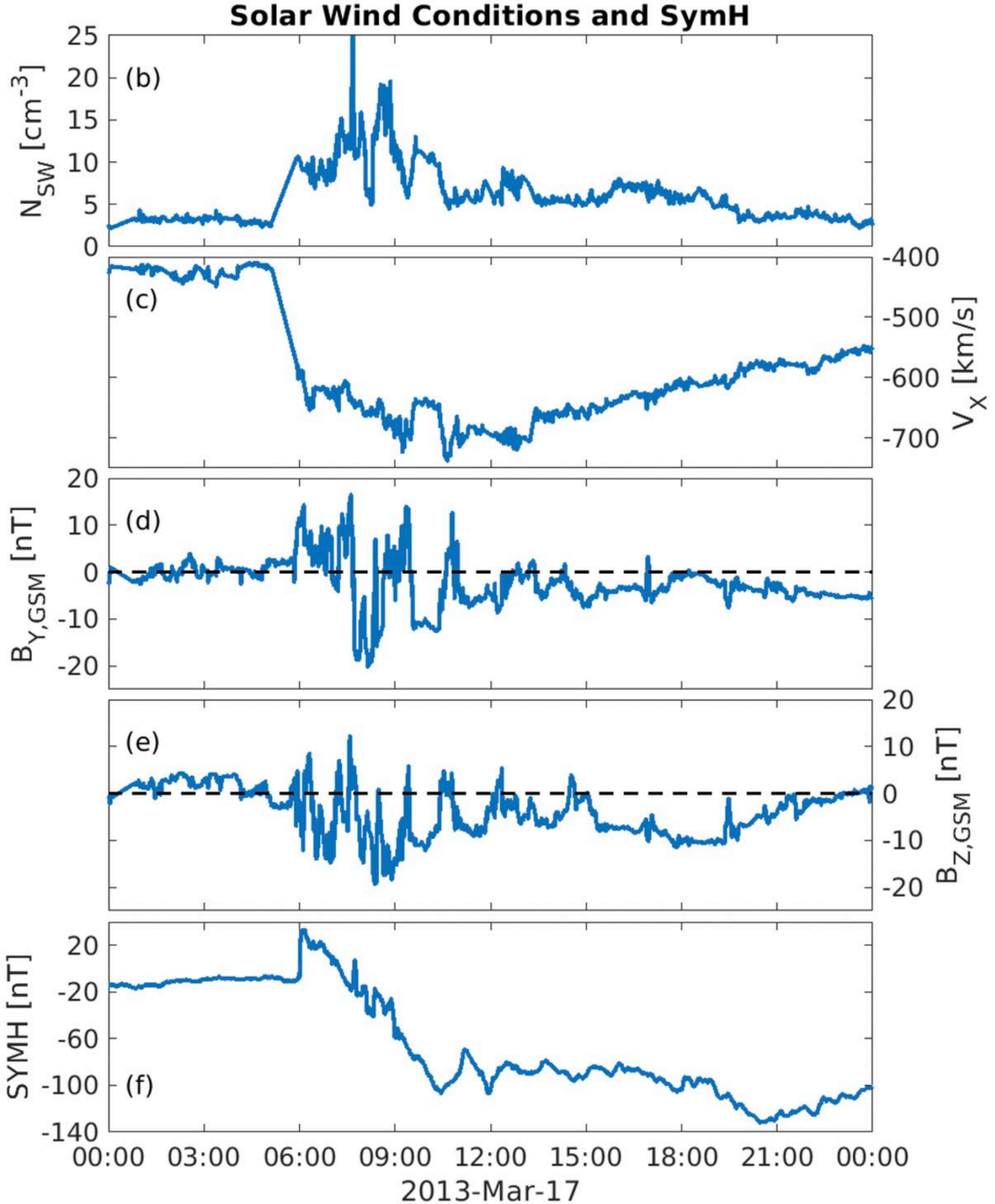

Figure 2.

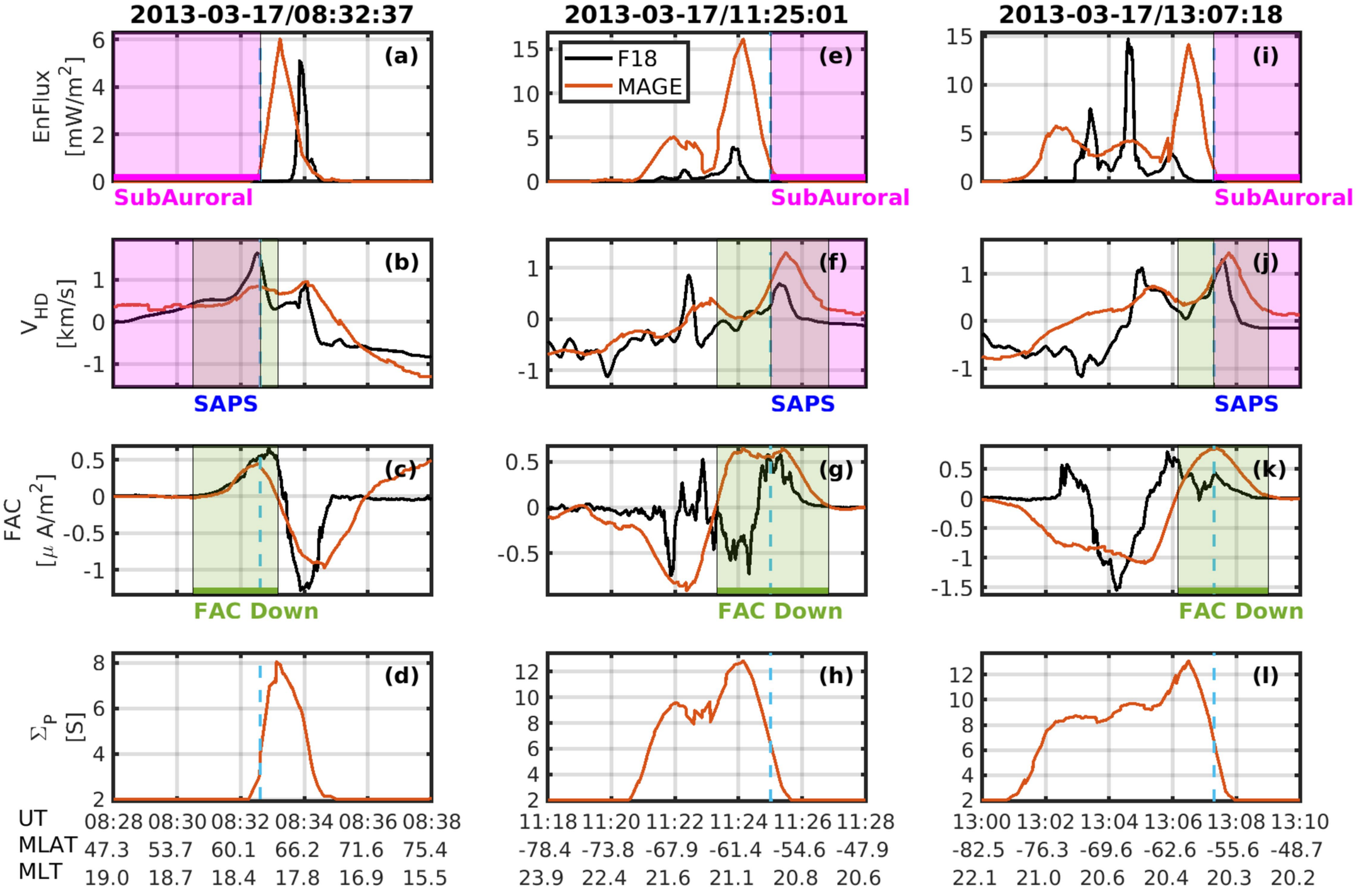
2013-03-17/08:32:37
2013-03-17/11:25:01
2013-03-17/13:07:18
F18
MAGE
EnFlux [mW/m^2]
V_{HD} [km/s]
FAC [μ A/m^2]
Σ_P [S]
(a)
(b)
(c)
(d)
(e)
(f)
(g)
(h)
(i)
(j)
(k)
(l)
SubAuroral
SAPS
FAC Down
UT 08:28 08:30 08:32 08:34 08:36 08:38
MLAT 47.3 53.7 60.1 66.2 71.6 75.4
MLT 19.0 18.7 18.4 17.8 16.9 15.5
11:18 11:20 11:22 11:24 11:26 11:28
-78.4 -73.8 -67.9 -61.4 -54.6 -47.9
23.9 22.4 21.6 21.1 20.8 20.6
13:00 13:02 13:04 13:06 13:08 13:10
-82.5 -76.3 -69.6 -62.6 -55.6 -48.7
22.1 21.0 20.6 20.4 20.3 20.2

Figure 3.

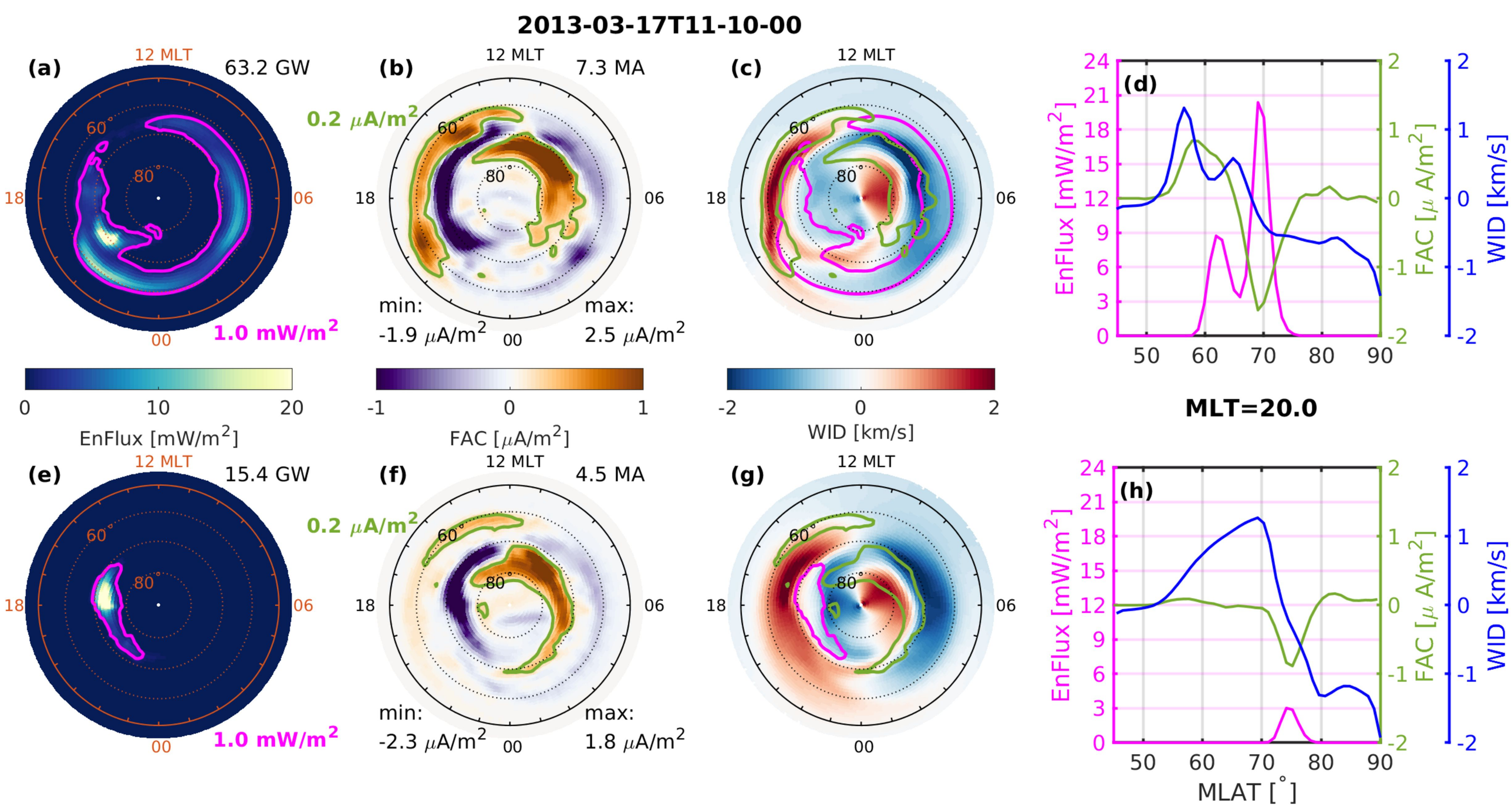
2013-03-17T11-10-00
(a)
12 MLT
63.2 GW
60°
80°
18
06
00
1.0 mW/m²
0
10
20
EnFlux [mW/m²]
(b)
12 MLT
7.3 MA
0.2 μA/m²
min:
-1.9 μA/m²
max:
2.5 μA/m²
-1
0
1
FAC [μA/m²]
(c)
12 MLT
-2
0
2
WID [km/s]
(d)
EnFlux [mW/m²]
FAC [μ A/m²]
WID [km/s]
MLT=20.0
(e)
12 MLT
15.4 GW
1.0 mW/m²
(f)
12 MLT
4.5 MA
0.2 μA/m²
min:
-2.3 μA/m²
max:
1.8 μA/m²
(g)
12 MLT
(h)
MLAT [°]

Figure 4.

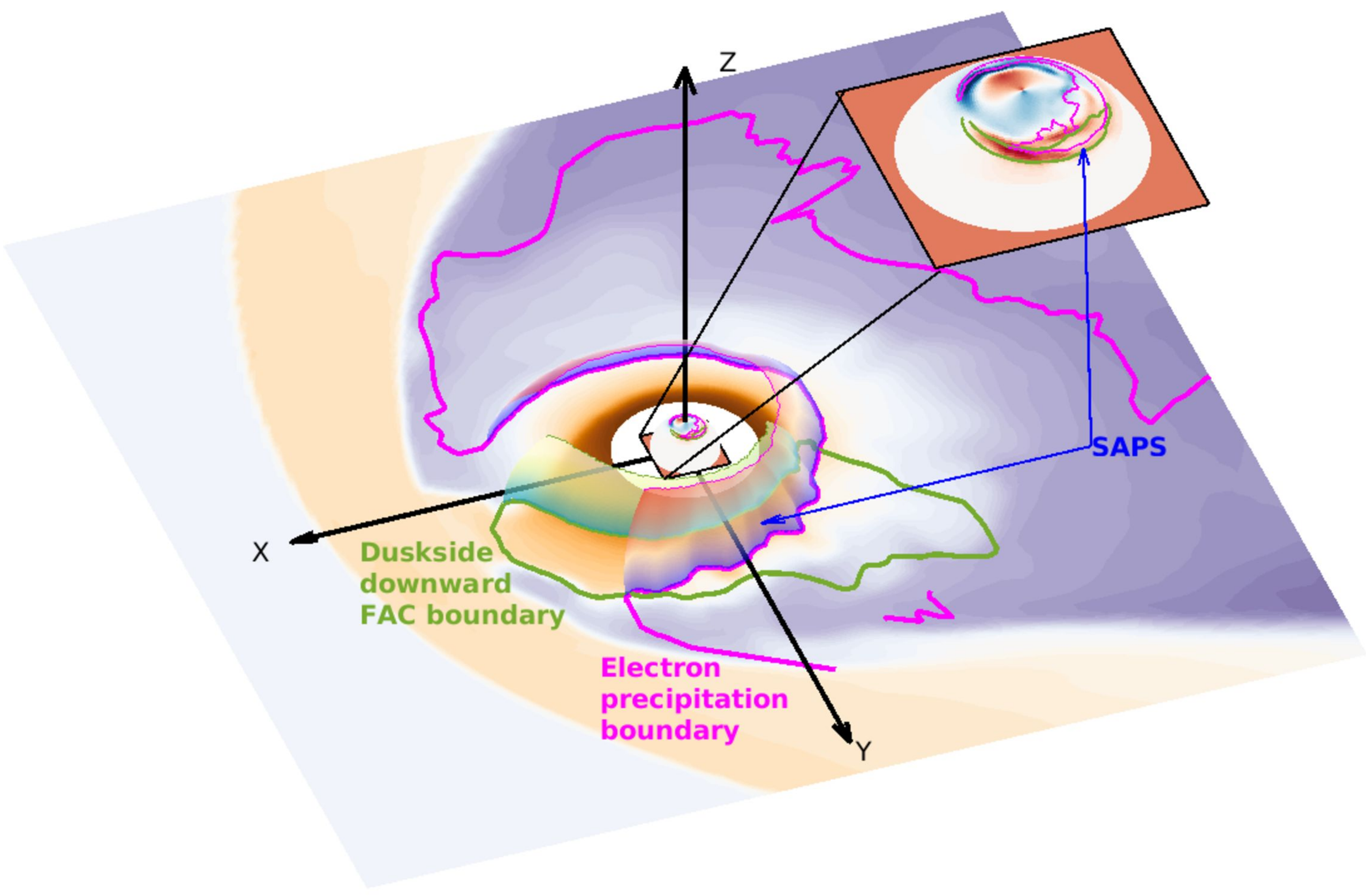
Z
X
Y
SAPS
Duskside
downward
FAC boundary
Electron
precipitation
boundary